Self-Sustained Visible-Light-Driven Electrochemical Redox Desalination

Karthick Ramalingam,[#] Mengjun Liang,[#] Ni Lar Win Pyae, Su Htike Aung, Than Zaw Oo, Pattarachai Srimuk, Jinxing Ma, Volker Presser,* Fuming Chen,* and T. David Waite

ACCESS | 📊 Metrics & More | 📰 Article Recommendations | 🆂🅸 Supporting Information

ABSTRACT: The freshwater scarcity and increasing energy demand are two challenging global issues. Herein, we propose a new route for desalination, self-sustained visible-light-driven electrochemical redox desalination. We propose a novel device architecture involving internal integration of a quasi-solid-state dye-sensitized solar cell and continuous redox-flow desalination units with a bifunctional platinized-graphite-paper electrode. Both the solar cell and redox-flow desalination units are integrated using the bifunctional electrode with one side facing the solar cell operating as a positive electrode and the other side facing the redox-flow desalination unit operating as a negative electrode. The solar cell contains a gel-based tri-iodide/iodide redox couple sandwiched between an N719 dye-modified photoanode and cathode. In contrast, the redox-flow desalination consists of re-circulating ferro/ferricyanide redox couple sandwiched between the anode and cathode with two salt streams located between these electrodes. The performances of bifunctional electrodes in both redox couples were thoroughly investigated by electrochemical characterization. The brackish feed can be continuously desalted to the freshwater level by utilizing visible light illumination. As a device, this architecture combines energy conversion and water desalination. This concept bypasses the need for electrical energy consumption for desalination, which provides a novel structural design using photodesalination to facilitate the development of self-sustained solar desalination technologies.

KEYWORDS: *water desalination, electrochemistry, solar technology, photoelectrochemistry, continuous desalination*
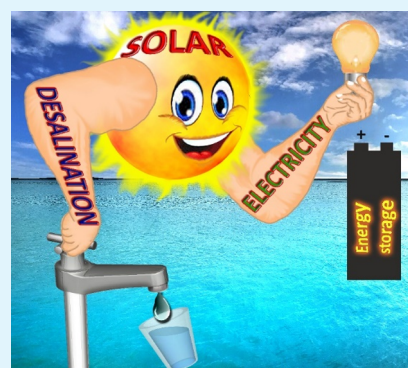
INTRODUCTION

Although 70% of our planet is covered with water, fresh water constitutes only 3% of this total water mass, and only a fraction is accessible for use.[1] Upon consideration of climate change, population growth, and economic requirements, it is estimated that 40% of the global population currently faces a severe water shortage,[1−3] with this proportion rising to 60% by 2025.[3,4] A variety of water desalination technologies now exist, including multistage flash distillation, multiple-effect distillation, reverse osmosis, electrodialysis, capacitive deionization, and desalination batteries.[5−7] All of these techniques require electrical energy.[8] Hence, the contribution of nonrenewable energy to most of our world's energy generation directly affects the possible sustainability of desalination. Most importantly, the aspect of sustainability is the energy efficiency and energy consumption of the desalination process, even when energy is provided by renewable sources. Electrochemical desalination technologies offer not only low energy consumption and high efficiency but also the ability to recover (at least partially) the invested energy during electrode regeneration.[9−13] This technology improves productivity due to low energy consumption, and also it is operated in the continuous mode of desalination.[14−17] As such, desalination cells may have a vital

dual use, stabilizing power grids and providing decentralized tools for energy management.[18−22]

Renewable energy systems such as solar thermal, solar photovoltaic, wind, and geothermal technologies have already been adopted to produce electrical/thermal energy for desalination systems.[23−26] Examples include desalination enabled by solar thermal, photovoltaic, wind, and geothermal energy.[27] Although renewable energy coupled with desalination systems is already available, further advances are required to sufficiently hybridize technologies, to enable fully continuous operation, and to improve the overall performance and design of these systems. Among them, solar-powered desalination becomes an efficient technology owing to solar-to-vapor conversion and solar-to-electricity conversion. There are several reports based on solar desalination by utilizing thermal energy. The black absorbed material is placed on the brackish water that generates the solar steam and leads to
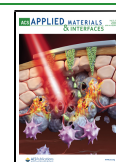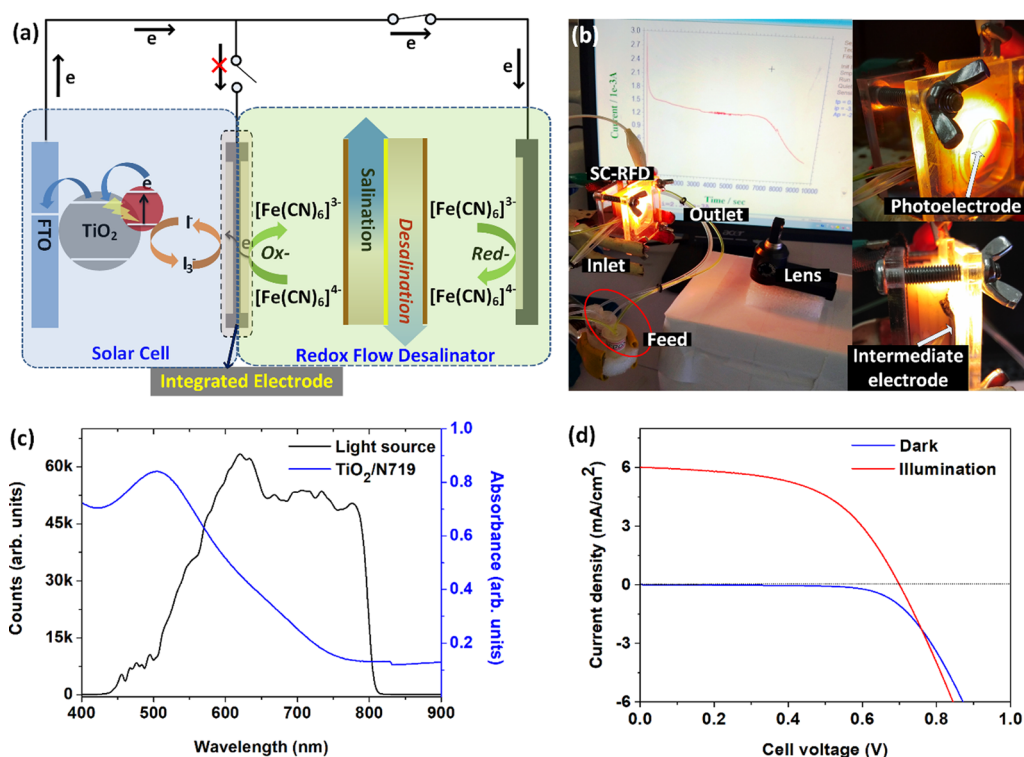
Figure 1. (a) Schematic diagram for the working principle of the integrated solar cell redo-flow desalination device; (b) photograph of the solar desalination device set-up with illumination; (c) comparison of absorption spectra of the continuous wavelength light source spot and the photoanode recorded at 400−900 nm; (d) I−V curve of the q-DSSC measured under dark and 108 mW/cm^2 light conditions.

evaporation. The solar thermal-based desalination has an excellent performance, but the cost of material and module fabrication is high during the industrial application.[28−33] Recently, the solar-to-electricity energy conversion, that is, solar-driven electrochemical desalination, is proposed for desalination purpose. For example, Liang et al. proposed a biophotoelectrochemical desalination cell that was fabricated with a biophotocatalyst anode and $K_3[Fe(CN)_6]$ catholyte.[34] Although the salt removal performance was promising, a nutrient medium was required to avoid the growth limitation of bacteria on the anode. More recently, Kim et al. proposed a three-functional device, including desalination, water treatment, and hydrogen production, that was powered by solar energy.[35] In this work, the photoanode was modified with a titania nanorod array such that photogenerated charge carriers facilitated ion transportation and resultant water desalination in the middle cell with a simultaneous generation of electricity. Due to chloride oxidation in this device, the overall pH value changes lead to reduced overall energy efficiency. In our recent report, we fabricated a photoredox desalination unit using a TiO_2 photoanode modified with an LEG4 dye and 4-hydroxy-2,2,6,6-tetramethylpiperidine 1-oxyl (TEMPO) redox electrolyte.[36] The photoanode is directly inserted into the redox electrolyte and captures electrons from the oxidation of the electrolyte. The salt ion can be extracted through ion-exchange membranes simultaneously. The desalination performance is very limited owing to the weak photocurrent, but the data served as an important proof-of-concept for direct photo-desalination in a redox medium.

Herein, we introduce the direct integration of a quasi-solid-state dye-synthesized solar cell (q-DSSC) and redox-flow desalination (RFD) unit. The integrated solar desalination device consists of three electrodes, including a photoelectrode

(anode), intermediate electrode, and counter electrode (cathode). We chose platinized graphite paper as the intermediate electrode where the redox electrolyte tri-iodide is reduced to iodide on the side of the solar cell; at the same time, on the redox-flow desalination unit side of the intermediate electrode, the ferro/ferricyanide redox process occurs to promote continuous salt removal. As long as a photocurrent is generated, desalination occurs in the redox-flow desalination unit, while energy is produced by the solar cell. In this work, the brackish water (ca. 4000 ppm) can be continuously desalted to freshwater levels when the solar cell anode is exposed to visible light. While very much in the early stages of development, our proof-of-concept unit demonstrates the ability to integrate renewable energy generation and salt removal fully.

Design, Structure, and Function of the Integrated Solar Desalination Unit. We fabricated an all-in-one solar desalination device by integrating the solar cell and redox-flow desalination units into a single device based on a three-electrode configuration. An internal photoelectrochemical desalination mechanism process is shown in Figure 1a. The solar desalination device is analogous to photosupercapacitor or photobattery architectures and operation principles.[37−39] Meanwhile, the present technology is most different from solar cell-integrated redox-flow batteries,[40,41] where the continuous desalination process occurred by consuming the photocurrent directly into the single device. The three electrodes used in the solar desalination system are a photoelectrode, an intermediate electrode, and a counter electrode with these electrodes arranged into a single compartment as displayed in Figure S1. The intermediate electrode is a graphite paper that is platinized on both sides. It serves as the positive electrode for the solar cell part to constantly reduce tri-iodide species and as the

negative electrode for the redox-flow desalination part to oxidize the ferrocyanide species. The solar cell and redox-flow desalination devices share a single platinized graphite paper as the intermediate electrode that performs a dual role: when a photon excites the N719 dye molecule to the lowest unoccupied molecular orbital (LUMO) level followed by transport to the conduction band of TiO_2, the charge is transported to the counter electrode of the redox-flow desalination device through an external circuit. Simultaneously, the excited dye is reduced by iodide species via the electron supplied by redox-flow desalination as a result of the oxidation of ferricyanide ions at the intermediate electrode (Figure 1a).

The concept of the solar desalination device is shown in Figure S2a. The solar cell and redox-flow desalination compartments employ electrodes with different relative spacings. A photograph of the complete solar desalination device setup is shown in Figure 1b, where the distance between the photoelectrode and the intermediate electrode is around 60 μm (solar cell), and the distance between the intermediate electrode and the counter electrode is 12 mm. In total, the device thickness is 1.3 cm between the photoelectrode and counter electrode for the complete solar desalination device. The design of the compartments and the associated salt and redox-flow streams are shown in Figure S2a,b. The volume of the redox-flow desalination part is about 0.3 cm^3; as such, 300 μL of the ferro/ferricyanide redox couple is held within the redox-flow desalination compartment with the NaCl electrolyte constantly flowing between the two cation and anion exchange membrane-bound compartments (thickness of each stream compartment is 0.3 cm). The active area of the membrane is 1×1 cm^2, and the active area of the photoelectrode, the intermediate electrode, and the counter electrode is each 0.49 cm^2, with the remaining part covered using parafilm (Figure S2b).

Figure 1c shows the comparison of the continuous wavelength light source (CWLS) output spectrum and the absorption spectrum of the photoelectrode (TiO_2/N719) between 400−900 nm. The photoelectrode absorption spectrum overlaps the CWLS spectrum between 400 and 800 nm with maximum photon absorption occurring between 550 and 600 nm. The current−voltage (I−V) curve measured under dark and illumination conditions with an intensity of 108 mW/cm^2 is shown in Figure 1d. The output light power density is obtained by adjusting the distance between the lens and solar desalination device (Table S1). Based on the above parameters, the q-DSSC device delivers an open circuit potential (V_{oc}) of 0.699 V, short-circuit specific current (I_{sc}) of 6 mA/cm^2, and fill factor (FF) of 54%. Hence, the obtained photovoltaic parameters are sufficient to supply electrical energy for redox-flow desalination due to the high photocurrent.

Electrochemical Enhancement of the Pt-Decorated Intermediate Electrode. The role of the intermediate electrode is to integrate the solar cell and redox-flow desalination parts into a single device, which is critical to the design and functionality of the solar desalination device. Electrochemical studies were conducted using three different materials as the intermediate electrode, namely, unmodified graphite paper (UGP), modified graphite paper (MGP), and platinized MGP (Pt-MGP). The detailed procedures for the fabrication of electrodes are given in the Experimental Section. Cyclic voltammograms show the electrochemical responses for the I_3^-/I^- and $[Fe(CN)_6]^{4-}/[Fe(CN)_6]^{3-}$ redox pairs (Figure

2a,b). From these data, we can quantify the peak-to-peak separation E_{pp} and the specific peak current at a particular
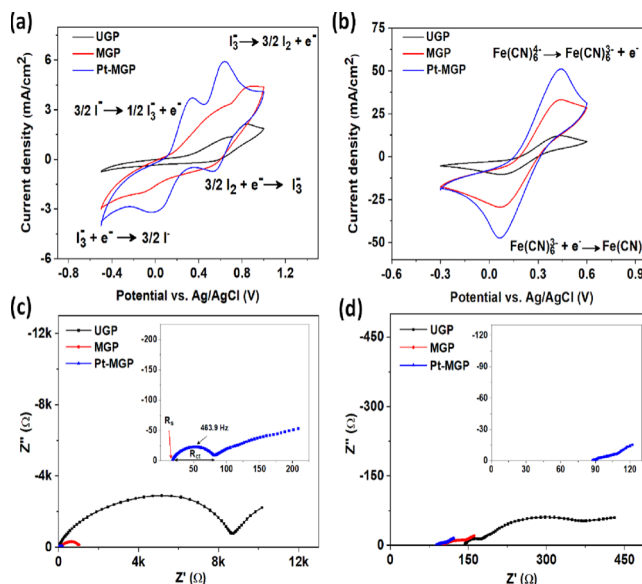

Figure 2. Three-electrode cyclic voltammetry of (a) tri-iodide/iodide redox couple and (b) $[Fe(CN)_6]^{4-}/[Fe(CN)_6]^{3-}$ redox couple using unmodified graphite paper (UGP), modified graphite paper (MGP), and platinum-decorated MGP (Pt-MGP) electrodes at a scan rate of 5 mV/s; Nyquist plot of symmetrical UGP, MGP, and Pt-MGP electrodes in the electrolyte of (c) tri-iodide/iodide redox couple and (d) $[Fe(CN)_6]^{4-}/[Fe(CN)_6]^{3-}$ redox couple measured from 100 kHz to 0.1 Hz at 0 V bias.

potential.[42] As can be seen from Figure 2a, two pairs of redox peaks are observed that correspond to the oxidation/reduction of I_3^-/I^- and I_2/I^- species, respectively. For comparison, the high specific current redox peaks are visible only after the surface treatment of UGP. This implies the improvement of charge transfer as well as a larger reactive area. The Pt-MGP has the highest redox specific current, compared to either MGP or UGP. As confirmed by the peak separation of each redox pair, Pt-MGP possesses the narrowest E_{pp} (0.324 V vs Ag/AgCl) with the highest areal current. Owing to the usage of organic electrolyte, there is no hydrogen evolution in the nonaqueous electrolyte.

For the integrated solar desalination device, the intermediate electrode is used as a bifunctional electrode, and we used cyclic voltammetry to characterize the $[Fe(CN)_6]^{4-}/[Fe(CN)_6]^{3-}$ redox couple (Figure 2b). There is a single pair of redox peaks that correspond to oxidation and reduction of $[Fe(CN)_6]^{4-/3-}$. The oxidation and reduction potentials of $[Fe(CN)_6]^{4-/3-}$ at 0.437 and 0.076 V are virtually identical for all the three intermediate electrode materials. Ferricyanide has been applied as a flow electrode for electrochemical desalination in the zinc/ferricyanide flow battery.[43] The corresponding specific current increases in the order of Pt-MGP>MGP>UGP, which infers an enhanced rate of the reaction. The Pt-MGP electrode exhibits high specific current in both the redox couples, compared to the other two intermediate electrode materials. Compared with the redox reaction of water, the oxidation potential of $[Fe(CN)_6]^{3-}$ is less than that required for oxygen evolution, while the reduction of $[Fe(CN)_6]^{4-}$ is higher than that required for hydrogen evolution. Hence, the ORR and HRR
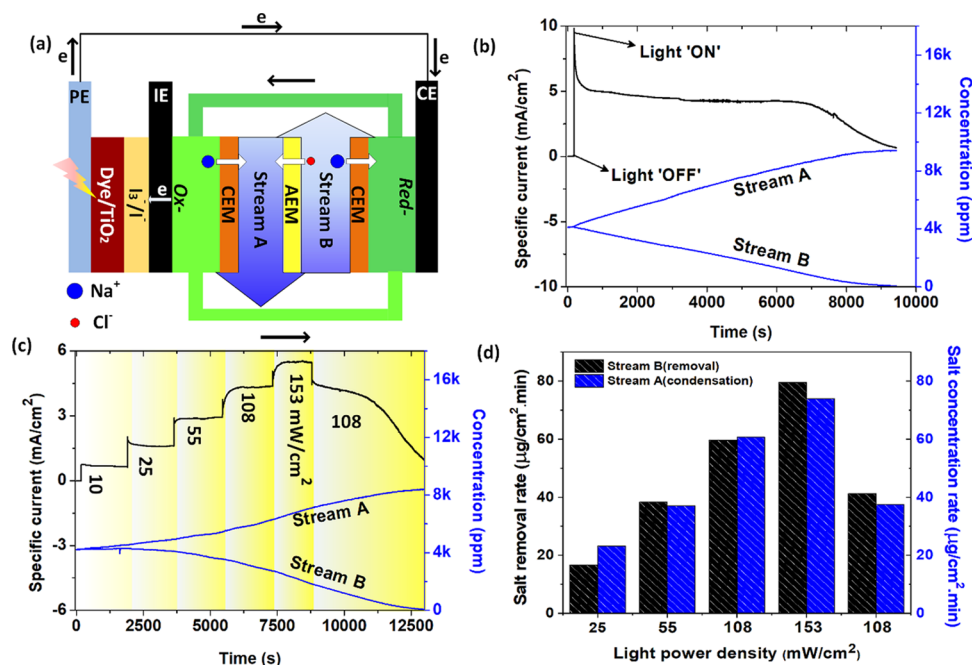
Figure 3. (a) Schematic diagram of the solar desalination device with the double salt stream; (b) photo-driven current discharge curve at zero bias and its corresponding concentration variation. (c) Photo-driven current discharge curve at zero bias with different intensities of the continuous wavelength light source output and its corresponding concentration measurement, and (d) salt removal/concentration rate in stream B/A with different intensities of the continuous wavelength light source output.
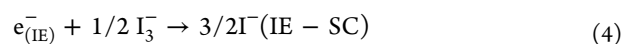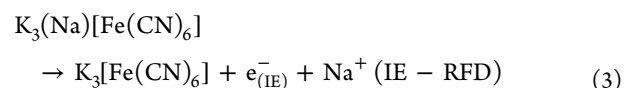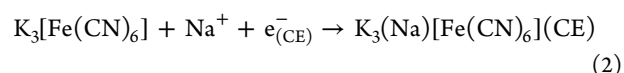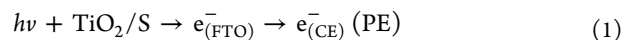
are negligible in the current system, which are consistent with previous reports.[44,45]

The charge transfer kinetics of the intermediate electrodes were analyzed by electrochemical impedance spectroscopy in a two-electrode configuration upon sandwiching the redox electrolyte between two identical electrodes, shown in Figure 2c,d and Tables S2 and S3. The R_s value varies (intercept of high frequency at the Z' axis) for all three electrodes with factors such as electrolyte resistance and the distance between two electrodes influencing the resistance. When comparing all the electrodes, Pt-MGP shows a low value of charge-transfer resistance (R_{ct}) with 66 and 21 Ω in I_3^-/I^- and $[Fe(CN)_6]^{4-}/[Fe(CN)_6]^{3-}$ redox couples, respectively. Hence, the Pt-MGP electrode/electrolyte interface exhibits the high charge transfer kinetics and electrochemical enhancement activity due to the surface roughness treatment and decoration with Pt. The current densities were improved in the Pt-MGP electrode due to the enhanced reactive sites, more contact, or high surface area, which is consistent with the results of the electrochemical impedance spectra.

Performance of the Integrated Solar Desalination Device. The solar desalination unit is operated by connecting the photoelectrode of the solar cell and the counter electrode of the redox-flow desalination, ensuring that the photoelectrode and intermediate electrode are disconnected. The redox-flow desalination process for continuous operation is similar to that described in our previous report.[15] The photocurrent is applied to the counter electrode at zero bias. In this system as shown in Figure 3a, the concentration of stream A increases due to the accumulation of Na$^+$ ions in the redox compartment near stream B. Concurrently, the Na$^+$ ion concentration decreases in stream B due to the cycling of this stream to the redox compartment near the intermediate electrode and the subsequent removal of Na$^+$ ions from this stream via transport through the cation exchange membrane.

Simultaneously, Cl$^-$ ions are transported through the anion exchange membrane from stream B to stream A to maintain charge balance. In this manner, an excess of Na$^+$ ions are generated within the redox reservoir adjacent to the counter electrode with these ions transported to the compartment of the intermediate electrode. Additionally, the oxidation of $[Fe(CN)_6]^{4-}$ to $[Fe(CN)_6]^{3-}$ occurs at the intermediate electrode with an excess of Na$^+$ ions transported to stream A through the cation exchange membrane. During this process, the redox electrolyte remains unchanged and can (theoretically) be used for long-term operation.

The processes of electron transfer, exchange of ions, and redox reactions occur at the photoelectrode, intermediate electrode, and counter electrode of the solar desalination device, as shown in Figure 1a. The variation in V_{oc} for different modes is shown in Figure S3. The V_{oc} in the solar cell and solar desalination modes are very similar in dark and light conditions, and no changes were observed in redox-flow desalination mode because the positive and negative electrodes of RFD are identical. Reactions that will occur for the various operational modes (i.e., the solar cell, redox-flow desalination, or combined solar desalination) are shown in Figures S4 and S5. These reactions demonstrate that the solar desalination device mode is light-responsive, as explained in Figure S6 and eqs 1−6.

$$hv + TiO_2/S \rightarrow e^-_{(FTO)} \rightarrow e^-_{(CE)} \; (PE) \tag{1}$$

$$K_3[Fe(CN)_6] + Na^+ + e^-_{(CE)} \rightarrow K_3(Na)[Fe(CN)_6](CE) \tag{2}$$

$$K_3(Na)[Fe(CN)_6]$$
$$\rightarrow K_3[Fe(CN)_6] + e^-_{(IE)} + Na^+ \; (IE - RFD) \tag{3}$$
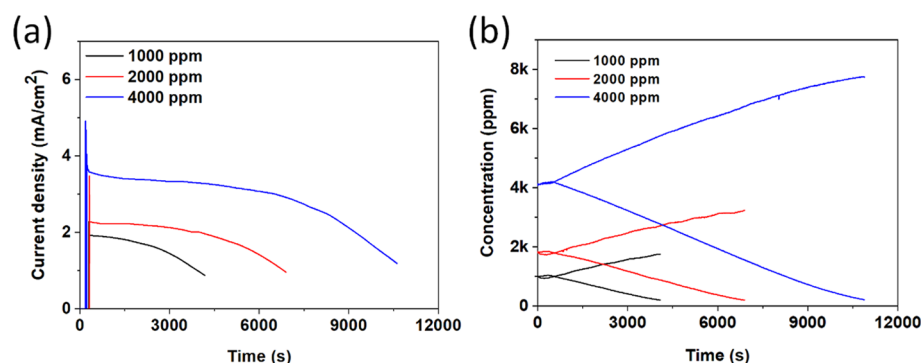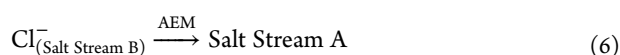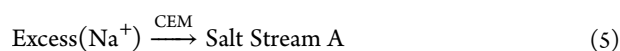
$$e^-_{(IE)} + 1/2 \, I_3^- \rightarrow 3/2 I^- (IE - SC) \tag{4}$$

Figure 4. (a) Photocurrent discharge curve variation upon the salt concentration and (b) corresponding concentration changes.

$$\text{Excess}(Na^+) \xrightarrow{\text{CEM}} \text{Salt Stream A} \qquad (5)$$

$$Cl^-_{(\text{Salt Stream B})} \xrightarrow{\text{AEM}} \text{Salt Stream A} \qquad (6)$$

The solar cell is illuminated using the CWLS with an intensity of 108 mW/cm² to provide the continuous desalination in short-circuit mode. Figure 3b shows the specific current vs time curve, which is driven by the solar-powered photocurrent and the respective concentration changes of streams A and B. Initially, the solar desalination device is operated in the dark, and no current flow is observed. When the device was irradiated by visible light, the specific current increased rapidly up to 4.8 mA/cm² and then suddenly falls to 3.5 mA/cm² and remained constant for several hours during desalination. The concentration of the effluent stream changes following the change in photocurrent. The salt concentration in stream B keeps on decreasing after illumination. At the initial stage, the salt content is high enough to maintain an excellent conductivity. It can be observed that the photocurrent declines very slowly. However, at the last stage of the desalination process, the major salt in stream B is transferred to the concentrated stream. The poor conductivity of stream B leads to the small photocurrent and hence the slow salt removal rate. Once the photocurrent begins to decrease gradually, the concentration decreases logarithmically instead of linearly with this change, indicating that the salt concentration is close to zero.

The desalination performance of the solar desalination device is based on the photocurrent. Complete desalination occurs after the treatment of UGP, as shown in Figure 3b and Figure S7a,b. The Pt-MGP electrode provides an excellent desalination performance owing to the high photocurrent delivered by the q-DSSC. The device using the MGP intermediate electrode consumes a net charge of 8.77 C to desalinate 4148 ppm within 4 h (Figure S7a). However, the device with the Pt-MGP electrode consumes a net charge of 10.78 C that reaches the freshwater level within a period of 2.9 h. However, the poor performance of the UGP-based solar desalination device makes it unfit for application as an intermediate electrode (Figure S7b). As shown in Figure S8, the enhanced photoelectrochemical desalination performance of the Pt-MGP is based on an improvement in the photovoltaic parameters of the q-DSSC. Overall SC-RFD performance is due to the improved reactive sites, electrode/electrolyte interfacial contact, and high surface area of Pt-MGP electrodes.

To reveal the desalination process with an effect of photocurrent, we performed the SC-RFD performance by monitoring with a stepwise increase of light intensity from 10

mW/cm² to 153 mW/cm². Figure 3c shows the photocurrent discharge curve of the solar desalination device operated at different light intensities. The specific photocurrent increased accordingly with the power intensity of the light, since the photocurrent is directly proportional to the light intensity. The charge consumption of SC-RFD at different light intensities is found to increase as follows: 0.29 C, 0.69 C, 1.29 C, and 1.98 C for 10, 25, 55, and 108 mW/cm², respectively. At a light intensity of 153 mW/cm², the charge consumption is low (1.95 C), compared to the power density of 108 mW/cm². This is because the period of illumination is minimized to 20 min for 153 mW/cm², since the salt removal rate is enhanced due to high photocurrent delivery. The current−voltage curve of the solar cell measured at different intensities is shown in Figure S9 that relates to the photocurrent discharge of the solar desalination unit. The concentration curve in Figure 3c shows a smaller gradient for stream A and stream B up to 55 mW/cm² and becomes more linear due to the high photocurrent delivery of the solar cell device. Hence, this proves that the process of desalination in the integrated SC-RFD device is based on the photocurrent (Table S4). The salt removal/condensation rates in the stream B/A are demonstrated in Figure 3d with the different specific powers of the light source. A high removal rate of 79.6 μg/min·cm² is obtained at a power density of 153 mW/cm². As such, the performance of the integrated solar desalination device is strongly dependent on the light intensity and solar cell parameters. The removal rate in stream B is approximately equal to the concentration rate in stream A, which reveals that the mass of exchanging ions at the condensing salt stream is balanced accordingly.

Solar Desalination Performance under the Various Concentrations of Salt Feed. Figure 4a shows the effect on photocurrent discharge when using different concentrations of NaCl, while the redox electrolyte concentration remained constant. The corresponding concentration curves of streams A and B are shown in Figure 4b. The consumption time increases for the high concentration salt feed. The time taken by the solar desalination device is 1.2, 2.0, and 2.9 h for desalination of salt streams with NaCl concentrations of 1000, 2000, and 4000 ppm, respectively. The salt removal rate varies accordingly with the obtained photocurrent at different NaCl concentrations due to changes in the conductivity of RFD electrolytes. As the intermediate electrode interconnects the q-DSSC cathode, an efficient charge transfer is required to reduce the tri-iodide for excellent photocurrent achievement. Hence, the concentration effect has dramatically influenced the photocurrent at various concentrations, and thus, the salt

removal rate varies. Subsequently, the energy consumption (E_c) was 0.12, 0.15, and 0.21 μmol/J for feed stream NaCl concentrations of 1000, 2000, and 4000 ppm, respectively, as shown in Figure S10. These data show that the desalination performance is affected by the salt concentration. Excellent desalination performance with a high salt removal rate is achieved for a feed stream salt concentration of 4000 ppm.

■ CONCLUSIONS

In summary, we have successfully fabricated an integrated solar desalination device that combines a continuous redox-flow desalination system and quasi-solid-state dye-sensitized solar cell in a single device. An intermediate Pt-modified graphite paper electrode integrates both systems into a single device that performs dual roles at both interfaces, that is, reduction of tri-iodide to iodide species in the solar cell and oxidation of ferricyanide to ferrocyanide in the redox-flow desalination unit. The redox potentials of the tri-iodide/iodide ($E_{1/2}$ = 0.324 V vs Ag/AgCl) and ferrocyanide/ferricyanide ($E_{1/2}$ = 0.361 V vs Ag/AgCl) redox couples are well matched for transportation of electrons from the redox-flow desalination to the solar cell through the intermediate electrode. The high performance of the solar desalination device results from the enhanced photocurrent of the intermediate electrode made from platinized modified graphite paper at both interfaces. The solar cell exhibits a V_{oc} of 0.7 V and I_{sc} of 6 mA/cm^2 at an input power intensity of 108 mW/cm^2 with the current supplied directly to the redox-flow desalination unit with short-circuit (zero bias). Overall, the solar desalination device performance is based on the solar cell parameters and the salt concentration in the feed stream. This device architecture provides a higher rate of photodesalination than any other system providing simultaneous energy harvesting and fresh-water production. While our work's data serve as an initial proof-of-concept at the bench scale only, the results obtained indicate that novel photodesalination technologies of the type presented here are worthy of further investigation.

■ EXPERIMENTAL SECTION

Fabrication of Intermediate Electrodes. A 2 × 5 cm^2 graphite paper (Jing Long TeTan Technologies; 0.5 mm thickness) was washed with acetone and water for later use. Both surfaces were treated by attaching adhesive tape and then stripped off. This was repeated five times and denoted as modified graphite paper (MGP) (Figure S11). Chloroplatinic acid (5 mM) in IPA was used to cover the MGP by drop-casting followed by heat treatment at 420 °C for 15 min (labeled as the Pt-MGP electrode). Both sides of these intermediate electrodes were masked with parafilm seals by leaving an active area of 0.5 cm^2 at the mid position.

Fabrication of the Solar Cell. Initially, the fluorine-doped tin oxide glasses (FTO; <10 Ω/sq) were sliced into 4 × 5 cm^2 pieces followed by surface cleaning using detergents, DI water, acetone, and isopropanol (IPA) (in this order). The cleaned FTO substrates were dried and subjected to blocking layer deposition by spin coating layers that contain 750 μL of titanium (IV) isopropoxide in 10 mL of ethanol. The blocking layer was annealed at 450 °C for 30 min. A TiO$_2$colloidal paste was prepared as follows: 0.6 g of TiO$_2$was added pinch by pinch over 0.1 g of polyethylene glycol and 10 mass % of polyethylene oxide in water followed by two drops of Triton-X 100 and 0.5 mL of acetylacetone and then ground for an hour. The prepared paste was sonicated and stirred for 12 h to obtain a homogenous solution. The obtained TiO$_2$ paste was applied on a buffer layer using a doctor blade and allowed to anneal at 150 °C for 15 min, +350 °C for 10 min, 450 °C for 15 min, and 500 °C for 30 min. After sintering, the electrode was treated in 40 mM TiCl$_4$ at a temperature of 70 °C for 0.5 h followed by heating at 500 °C for 1 h. The final compact TiO$_2$ photoanode was immersed in an acetonitrile solution containing 0.3 mM N719 dye for 24 h under dark conditions. The dye-modified TiO$_2$ layer was washed with ethanol several times to remove the unabsorbed dye molecules. The prepared photoanode was sealed with parafilm leaving an active area of 0.5 cm^2 in the middle. A drop of I$_2$/I$_3$$^-$ electrolyte was added before covering with graphite paper prepared as described above. The detailed preparation procedure for the I$_2$/I$_3$$^-$ electrolyte was as follows: 10 mM LiI, 1 mM I$_2$, 0.6 M 1-hexyl-3-methylimidazolium iodide, and 0.5 M 4-tert-butylpyridine were mixed in 2 mL of acetonitrile, and then, 10 mass % of poly(vinylidene fluoride-co-hexafluoropropylene) was added. The mixture was subsequently stirred overnight at 70 °C.

Fabrication of the Solar Desalination Device (Solar Cell-Redox-Flow Desalination). The solar desalination cell comprises four components as follows: two redox streams and two salt streams (A and B) with a solar cell (SC), an intermediate electrode (IE), and counter electrode (CE) electrodes. The configuration is as follows:

SC (IE) | RFD (redox) ‖ SS ‖ SS ‖ RFD (redox) | CE

where "|" detonates the separation of components, and "‖" represents the ion-exchange membranes (i.e., anion exchange membrane and cation exchange membrane, ASTOM Corporation; standard grade). The anion exchange membrane was placed between the two salt streams A and B. Two cation exchange membranes were placed at an intermediate electrode and counter electrode of the redox-flow desalination unit. The redox electrolyte contains a mixture of 80 mM potassium ferrocyanide and potassium ferricyanide with 4000 ppm of NaCl in an aqueous medium. The salt stream contains the same concentration of NaCl as in the redox medium. The salt volume was 2 mL, the flow rate was 4.15 mL/min, the active membrane area was 1 cm^2, and the thickness of the plate was 3 mm. As displayed in Figure S2b, the dimension of this compartment is 6.25 cm^2. In the center of this compartment, the square-cut area exposed to the electrolyte is about 1 cm^2. The electrolyte passes through the holes with a diameter of 1 mm at the edges of the hollow area.

Fabrication of the Symmetrical Dummy Cell for Electrochemical Characterization. All the intermediate electrodes were sliced into 3.0 × 1.5 cm^2 and masked with an active area of 0.5 cm^2 using a paraffin film. The fabrication of the cells is as follows:

(i) For solar cell intermediate electrodes: The two identical intermediate electrodes were sandwiched with the redox electrolyte that contains 10 mass % polyvinylidene fluoride/hexafluoropropylene polymer, 1 mM iodine, 10 mM lithium iodide, 0.5 M tert-butyl pyridine, and 0.6 M 1-hexyl-3-methylimidazolium iodide in acetonitrile. Then, it is annealed at 70 °C to melt the paraffin.

(ii) For redox-flow desalination: the redox-flow desalination device was fabricated in the configuration given below:

IE | Ferro/ferricyanide ‖ NaCl ‖ NaCl ‖ ferro/ferricyanide | IE

where "|" represents the component separation and "‖" represents the exchange membrane.

■ CHARACTERIZATION

The UV−vis absorbance was measured by using a SHIMADZU Corporation (UV 2600) spectrometer and recorded over the wavelength range 400−900 nm. The spectra of the CWLS were measured using a YSL Photonics instrument.

Electrochemical Characterization. All electrochemical characterizations were carried out with a CHI760E (A18470) electrochemical workstation. Cyclic voltammetry was conducted in a three-electrode configuration as follows: the intermediate electrode as the working electrode, platinum mesh as the counter electrode, and Ag/AgCl as the reference electrode. The potential was recorded between −0.5 to +1.0 V and −0.3 to +0.6 V in I$_3$$^-$/I$^-$ and [Fe(CN)$_6$]$^{4-}$/[Fe(CN)$_6$]$^{3-}$ redox couples, respectively, at a scan rate of 5 mV/s. The same

concentration of electrolyte was employed for the intermediate electrode of the redox-flow desalination side. For the intermediate electrode of the solar cell side, the electrolyte contained 10 mM LiI, and 1 mM I_2, and 0.1 M LiClO$_4$ in acetonitrile and purged in N_2 gas for 30 min before characterization. Two electrode configurations were employed for electrochemical impedance spectroscopy with the two identical electrodes sandwiched between the electrolytes. The redox electrolyte for the solar cell characterization contained a similar content to that used for solar cell fabrication.

Electrochemical impedance spectra were measured in the frequency range of 100 kHz to 1 Hz at zero bias for both the redox media: R_s series resistance (intercept of high frequency at the Z' axis) and R_{ct} (intercept of the semicircle circle in a high-frequency range). The C_{dl} is extracted from ω_{max} in a higher frequency range using

$$C_{dl} = \frac{1}{2\pi f Z''}$$

where C_{dl} is the electrical double-layer capacitance (F), f is the frequency (Hz), and Z'' is the intercept of the maximum frequency of the semicircle (Ω).

Photovoltaic Characterization. A continuous wavelength light source between 400 and 800 nm was utilized to illuminate the dye-synthesized solar cell. The intensity of specific power was adjusted by the percentage of amplitude. The I−V curve was measured using an electrochemical workstation with recordings between 0 and 0.9 V. The solar cell parameters may be extrapolated from the I−V curves (Figure S12).

$$FF\% = \frac{V_{max} \times I_{max}}{V_{oc} \times I_{sc}}$$

where FF is the fill factor, V_{max} is the maximum voltage (V), I_{max} is the maximum photocurrent (mA), V_{oc} is the open-circuit potential (V), and I_{sc} is the short-circuit photocurrent (A).

$$PCE\% = \frac{V_{oc} \times I_{sc} \times FF}{P_{in}}$$

Where PCE is the power conversion efficiency, and P_{in} is the power of the input light (W).

Solar Desalination Characterization. The current−time technique was utilized to analyze the photocurrent discharge from the solar cell to the redox-flow desalination device. The positive electrode and negative electrode were connected at the photoelectrode of the solar cell and the counter electrode of the redox-flow desalination, respectively. The intermediate electrode terminal was disconnected. The salt removal rate can be calculated using the below equation:

$$SRR = \frac{(C_i - C_f) * V}{T * A_{cell}}$$

Where C_i and C_f are the concentrations of NaCl during the initial and final experiments (mg/L); V is the total volume of NaCl used (L), and T is the time taken to desalinate. A_{cell} is the area of the active surface.

The energy consumption is calculated as follows:

$$E_C = \frac{(C_i - C_f) \times V}{MM \times P \times A \times t_p}$$

where P is the specific power of the light (W/cm^2); A is the active area of the electrodes (cm^2), MM stands for the molar mass of NaCl, and t_p is the time taken to illuminate the device (s). The charge consumption (Coulombs, Q) is the integral of the I−t curve.

■ ASSOCIATED CONTENT

ⓢ Supporting Information

The Supporting Information is available free of charge at https://pubs.acs.org/doi/10.1021/acsami.0c08286.

> Solar desalination components; experimental set up; the reaction mechanism; the performance of the solar device and solar redox desalination device (PDF)

■ AUTHOR INFORMATION

Corresponding Authors

> **Volker Presser** − *INM - Leibniz Institute for New Materials, 66123 Saarbrücken, Germany; Department of Materials Science & Engineering, Saarland University, 66123 Saarbrücken, Germany;* Email: volker.presser@leibniz-inm.de
> **Fuming Chen** − *Guangdong Provincial Key Laboratory of Quantum Engineering and Quantum Materials, Guangdong Engineering Technology Research Center of Efficient Green Energy and Environment Protection Materials, School of Physics and Telecommunication Engineering, South China Normal University, Guangzhou 510006, PR China;* ⓘ orcid.org/0000-0002-0108-9831; Email: fmchen@m.scnu.edu.cn

Authors

> **Karthick Ramalingam** − *Guangdong Provincial Key Laboratory of Quantum Engineering and Quantum Materials, Guangdong Engineering Technology Research Center of Efficient Green Energy and Environment Protection Materials, School of Physics and Telecommunication Engineering, South China Normal University, Guangzhou 510006, PR China*
> **Mengjun Liang** − *Guangdong Provincial Key Laboratory of Quantum Engineering and Quantum Materials, Guangdong Engineering Technology Research Center of Efficient Green Energy and Environment Protection Materials, School of Physics and Telecommunication Engineering, South China Normal University, Guangzhou 510006, PR China*
> **Ni Lar Win Pyae** − *Guangdong Provincial Key Laboratory of Quantum Engineering and Quantum Materials, Guangdong Engineering Technology Research Center of Efficient Green Energy and Environment Protection Materials, School of Physics and Telecommunication Engineering, South China Normal University, Guangzhou 510006, PR China*
> **Su Htike Aung** − *Department of Physics, Materials Sciences Research Laboratory, University of Mandalay, 05032 Mandalay, Myanmar*
> **Than Zaw Oo** − *Department of Physics, Materials Sciences Research Laboratory, University of Mandalay, 05032 Mandalay, Myanmar*
> **Pattarachai Srimuk** − *INM - Leibniz Institute for New Materials, 66123 Saarbrücken, Germany; Department of Materials Science & Engineering, Saarland University, 66123 Saarbrücken, Germany*
> **Jinxing Ma** − *UNSW Water Research Centre, School of Civil and Environmental Engineering, University of New South Wales, Sydney, New South Wales 2052, Australia;* ⓘ orcid.org/0000-0002-5087-3972

T. David Waite − *UNSW Water Research Centre, School of Civil and Environmental Engineering, University of New South Wales, Sydney, New South Wales 2052, Australia;*
ⓘ orcid.org/0000-0002-5411-3233

■ REFERENCES

(1) Jones, E.; Qadir, M.; van Vliet, M. T. H.; Smakhtin, V.; Kang, S. M. The State of Desalination and Brine Production: A Global Outlook. *Sci. Total Environ.* **2019**, *657*, 1343−1356.

(2) Abdelkareem, M. A.; El Haj Assad, M.; Sayed, E. T.; Soudan, B. Recent Progress in The Use of Renewable Energy Sources to Power Water Desalination Plants. *Desalination* **2018**, *435*, 97−113.

(3) Darre, N. C.; Toor, G. S. Desalination of Water: A Review. *Curr. Pollut. Rep.* **2018**, *4*, 104−111.

(4) Alkaisi, A.; Mossad, R.; Sharifian-Barforoush, A. A Review of The Water Desalination Systems Integrated with Renewable Energy. *Energy Procedia* **2017**, *110*, 268−274.

(5) Suss, M. E.; Presser, V. Water Desalination with Energy Storage Electrode Materials. *Joule* **2018**, *2*, 10−15.

(6) Werber, J. R.; Osuji, C. O.; Elimelech, M. Materials for Next-generation Desalination and Water Purification Membranes. *Nat. Rev. Mater.* **2016**, *1*, 16018.

(7) Srimuk, P.; Su, X.; Yoon, J.; Aurbach, D.; Presser, V. Charge-transfer Materials for Electrochemical Water Desalination, Ion Separation and the Recovery of Elements. *Nat. Rev. Mater.* **2020**, DOI: 10.1038/s41578-020-0193-1.

(8) Shatat, M.; Riffat, S. B. Water Desalination Technologies Utilizing Conventional and Renewable Energy Sources. *Int. J. Low-Carbon Technol.* **2012**, *9*, 1−19.

(9) Hawks, S. A.; Ramachandran, A.; Porada, S.; Campbell, P. G.; Suss, M. E.; Biesheuvel, P. M.; Santiago, J. G.; Stadermann, M. Performance Metrics for The Objective Assessment of Capacitive Deionization Systems. *Water Res.* **2019**, *152*, 126−137.

(10) Li, Z.; Wang, C.; Su, J.; Ling, S.; Wang, W.; An, M. Fast-Growing Field of Interfacial Solar Steam Generation: Evolutional Materials, Engineered Architectures, and Synergistic Applications. *Solar RRL* **2019**, *3*, 1800206.

(11) Nam, D. H.; Choi, K. S. Tandem Desalination/Salination Strategies Enabling the Use of Redox Couples for Efficient and Sustainable Electrochemical Desalination. *ACS Appl. Mater. Interfaces* **2019**, *11*, 38641−38647.

(12) Dai, J.; Win Pyae, N. L.; Chen, F.; Liang, M.; Wang, S.; Ramalingam, K.; Zhai, S.; Su, C.-Y.; Shi, Y.; Tan, S. C.; Zhang, L.; Chen, Y. Zinc−Air Battery-Based Desalination Device. *ACS Appl. Mater. Interfaces* **2020**, *12*, 25728−25735.

(13) Dai, J.; Wang, J.; Hou, X.; Ru, Q.; He, Q.; Srimuk, P.; Presser, V.; Chen, F. Dual-Zinc Electrode Electrochemical Desalination. *ChemSusChem* **2020**, *13*, 2792−2798.

(14) Beh, E. S.; Benedict, M. A.; Desai, D.; Rivest, J. B. A Redox-Shuttled Electrochemical Method for Energy-Efficient Separation of Salt from Water. *ACS Sustainable Chem. Eng.* **2019**, *7*, 13411−13417.

(15) Wang, J.; Zhang, Q.; Chen, F.; Hou, X.; Tang, Z.; Shi, Y.; Liang, P.; Yu, D. Y. W.; He, Q.; Li, L.-J. Continuous Desalination with A Metal-free Redox-mediator. *J. Mater. Chem. A* **2019**, *7*, 13941−13947.

(16) Chen, F.; Wang, J.; Ru, Q.; Aung, S. H.; Oo, T. Z.; Chu, B. Continuous Electrochemical Desalination via a Viologen Redox Flow Reaction. *J. Electrochem. Soc.* **2020**, *167*, No. 083503.

(17) Zhang, Q.; Aung, S. H.; Oo, T. Z.; Chen, F. Continuous Electrochemical Deionization by Utilizing the Catalytic Redox Effect of Environmentally Friendly Riboflavin-5′-phosphate Sodium. *Mater. Today Commun.* **2020**, *23*, 100921.

(18) Zhao, Y.; Waterhouse, G. I. N.; Chen, G.; Xiong, X.; Wu, L.-Z.; Tung, C.-H.; Zhang, T. Two-dimensional-related catalytic materials for solar-driven conversion of CO x into valuable chemical feedstocks. *Chem. Soc. Rev.* **2019**, *48*, 1972−2010.

(19) Zhao, W.; Guo, L.; Ding, M.; Huang, Y.; Yang, H. Y. Ultrahigh-Desalination-Capacity Dual-Ion Electrochemical Deionization Device Based on Na3V2(PO4)3@C-AgCl Electrodes. *ACS Appl. Mater. Inyerfaces* **2018**, *10*, 40540−40548.

(20) Chen, F.; Huang, Y.; Guo, L.; Sun, L.; Wang, Y.; Yang, H. Y. Dual-ions Electrochemical Deionization: A Desalination Generator. *Energy Environ. Sci.* **2017**, *10*, 2081−2089.

(21) Lee, J.; Srimuk, P.; Fleischmann, S.; Su, X.; Hatton, T. A.; Presser, V. Redox-electrolytes for Non-flow Electrochemical Energy Storage: A Critical Review and Best Practice. *Prog. Mater. Sci.* **2019**, *101*, 46−89.

(22) Lee, J.; Srimuk, P.; Zornitta, R. L.; Aslan, M.; Mehdi, B. L.; Presser, V. High Electrochemical Seawater Desalination Performance Enabled by an Iodide Redox Electrolyte Paired with a Sodium Superionic Conductor. *ACS Sustainable Chem. Eng.* **2019**, *7*, 10132−10142.

(23) Tao, P.; Ni, G.; Song, C.; Shang, W.; Wu, J.; Zhu, J.; Chen, G.; Deng, T. Solar-driven Interfacial Evaporation. *Nat. Energy* **2018**, *3*, 1031−1041.

(24) Elsheikh, A. H.; Sharshir, S. W.; Mostafa, M. E.; Essa, F. A.; Ahmed Ali, M. K. Applications of Nanofluids in Solar Energy: A Review of Recent Advances. *Renew. Sust. Energ. Rev.* **2018**, *82*, 3483−3502.

(25) Ghaffour, N.; Lattemann, S.; Missimer, T.; Ng, K. C.; Sinha, S.; Amy, G. Renewable Energy-driven Innovative Energy-efficient Desalination Technologies. *Appl. Energy* **2014**, *136*, 1155−1165.

(26) Ali, A.; Tufa, R. A.; Macedonio, F.; Curcio, E.; Drioli, E. Membrane Technology in Renewable-Energy-driven Desalination. *Renew. Sust. Energ. Rev.* **2018**, *81*, 1−21.

(27) Al-Karaghouli, A.; Kazmerski, L. L. Energy Consumption and Water Production Cost of Conventional and Renewable-energy-powered Desalination Processes. *Renew. Sust. Energ. Rev.* **2013**, *24*, 343−356.

(28) Zhang, Y.; Xiong, T.; Nandakumar, D. K.; Tan, S. C. Structure Architecting for Salt-Rejecting Solar Interfacial Desalination to Achieve High-Performance Evaporation With In Situ Energy Generation. *Adv. Sci.* **2020**, *7*, 1903478.

(29) Xu, Z.; Zhang, L.; Zhao, L.; Li, B.; Bhatia, B.; Wang, C.; Wilke, K. L.; Song, Y.; Labban, O.; Lienhard, J. H.; Wang, R.; Wang, E. N. Ultrahigh-efficiency Desalination via A Thermally-localized Multistage Solar Still. *Energy Environ. Sci.* **2020**, *13*, 830−839.

(30) Zhang, Y.; Ravi, S. K.; Vaghasiya, J. V.; Tan, S. C. A Barbeque-Analog Route to Carbonize Moldy Bread for Efficient Steam Generation. *iScience* **2018**, *3*, 31−39.

(31) Zhang, Y.; Ravi, S. K.; Tan, S. C. Food-derived Carbonaceous Materials for Solar Desalination and Thermo-electric Power Generation. *Nano Energy* **2019**, *65*, 104006.

(32) Zhang, Y.; Ravi, S. K.; Tan, S. C. Systematic Study of the Effects of System Geometry and Ambient Conditions on Solar Steam Generation for Evaporation Optimization. *Adv. Sustain. Syst.* **2019**, *3*, 1900044.

(33) Nandakumar, D. K.; Zhang, Y.; Ravi, S. K.; Guo, N.; Zhang, C.; Tan, S. C. Solar Energy Triggered Clean Water Harvesting from Humid Air Existing above Sea Surface Enabled by a Hydrogel with Ultrahigh Hygroscopicity. *Adv. Mater.* **2019**, *31*, No. e1806730.

(34) Liang, Y.; Feng, H.; Shen, D.; Li, N.; Long, Y.; Zhou, Y.; Gu, Y.; Ying, X.; Dai, Q. A High-performance Photo-microbial Desalination Cell. *Electrochim. Acta* **2016**, *202*, 197−202.

(35) Kim, S.; Piao, G.; Han, D. S.; Shon, H. K.; Park, H. Solar Desalination Coupled with Water Remediation and Molecular Hydrogen Production: A Novel Solar Water-energy Nexus. *Energy Environ. Sci.* **2018**, *11*, 344−353.

(36) Chen, F.; Karthick, R.; Zhang, Q.; Wang, J.; Liang, M.; Dai, J.; Jiang, X.; Jiang, Y. Exploration of A Photo-redox Desalination Generator. *J. Mater. Chem. A* **2019**, *7*, 20169−20175.

(37) Das, A.; Deshagani, S.; Kumar, R.; Deepa, M. Bifunctional Photo-Supercapacitor with a New Architecture Converts and Stores Solar Energy as Charge. *ACS Appl. Mater. Interfaces* **2018**, *10*, 35932−35945.

(38) Yun, S.; Qin, Y.; Uhl, A. R.; Vlachopoulos, N.; Yin, M.; Li, D.; Han, X.; Hagfeldt, A. New-generation Integrated Devices Based on Dye-sensitized and Perovskite Solar Cells. *Energy Environ. Sci.* **2018**, *11*, 476−526.

(39) Guo, W.; Xue, X.; Wang, S.; Lin, C.; Wang, Z. L. An Integrated Power Pack of Dye-sensitized Solar Cell and Li Battery Based on Double-sided TiO2 Nanotube Arrays. *Nano Lett.* **2012**, *12*, 2520−2523.

(40) Wedege, K.; Bae, D.; Smith, W. A.; Mendes, A.; Bentien, A. Solar Redox Flow Batteries with Organic Redox Couples in Aqueous Electrolytes: A Minireview.pdf. *J. Phys. Chem. C* **2018**, *122*, 25729−25740.

(41) Gao, L.; Zhang, X.; Zhao, X.; Tao, S.; Lu, J. Solar-charging Aqueous Redox Flow Battery with Optimal Redox Couple Combination. *Chem. Lett.* **2020**, *49*, 248−251.

(42) Wu, J.; Lan, Z.; Lin, J.; Huang, M.; Huang, Y.; Fan, L.; Luo, G.; Lin, Y.; Xie, Y.; Wei, Y. Counter Electrodes in Dye-sensitized Solar Cells. *Chem. Soc. Rev.* **2017**, *46*, 5975−6023.

(43) Desai, D.; Beh, E. S.; Sahu, S.; Vedharathinam, V.; van Overmeere, Q.; de Lannoy, C. F.; Jose, A. P.; Völkel, A. R.; Rivest, J. B. Electrochemical Desalination of Seawater and Hypersaline Brines with Coupled Electricity Storage. *ACS Energy Lett.* **2018**, *3*, 375−379.

(44) Marichelvam, T.; Manzoor Bhat, Z.; Thimmappa, R.; Devendrachari, M. C.; Kottaichamy, A. R.; Naranammalpuram Sundaram, V. N.; Thotiyl, M. O. Hydrogen Fuel Exhaling Zn−Ferricyanide Redox Flow Battery. *ACS Sustainable Chem. Eng.* **2019**, *7*, 16241−16246.

(45) Pinhassi, R. I.; Kallmann, D.; Saper, G.; Dotan, H.; Linkov, A.; Kay, A.; Liveanu, V.; Schuster, G.; Adir, N.; Rothschild, A. Hybrid Bio-photo-electro-chemical Cells for Solar Water Splitting. *Nat. Commun.* **2016**, *7*, 12552.